

Effects of electron recirculation on a hard x-ray source observed during the interaction of a high intensity laser pulse with thin Au targets

A. Compant La Fontaine, C. Courtois, E. Lefebvre, J. L. Bourgade, O. Landoas, K. Thorp, and C. Stoeckl

Citation: *Physics of Plasmas* **20**, 123111 (2013); doi: 10.1063/1.4848759

View online: <http://dx.doi.org/10.1063/1.4848759>

View Table of Contents: <http://scitation.aip.org/content/aip/journal/pop/20/12?ver=pdfcov>

Published by the *AIP Publishing*

Articles you may be interested in

[Interaction of high intensity laser with non-uniform clusters and enhanced X-ray emission](#)

Phys. Plasmas **21**, 103101 (2014); 10.1063/1.4897188

[K \$\alpha\$ and bremsstrahlung x-ray radiation backlighter sources from short pulse laser driven silver targets as a function of laser pre-pulse energy](#)

Phys. Plasmas **21**, 031211 (2014); 10.1063/1.4865230

[Characterisation of a MeV Bremsstrahlung x-ray source produced from a high intensity laser for high areal density object radiography](#)

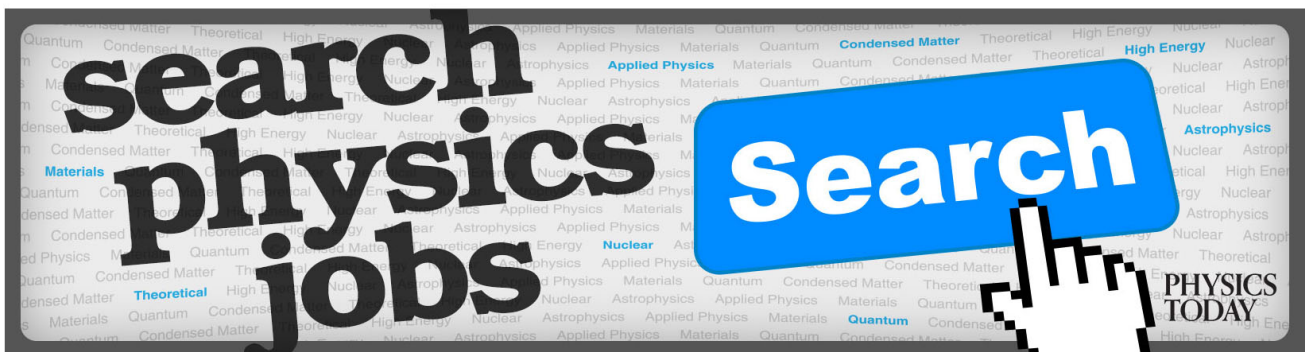
Phys. Plasmas **20**, 083114 (2013); 10.1063/1.4818505

[Production of multi-MeV Bremsstrahlung x-ray sources by petawatt laser pulses on various targets](#)

Phys. Plasmas **19**, 023104 (2012); 10.1063/1.3680611

[Absolute energy distribution of hard x rays produced in the interaction of a kilohertz femtosecond laser with tantalum targets](#)

Rev. Sci. Instrum. **77**, 093302 (2006); 10.1063/1.2337086



Effects of electron recirculation on a hard x-ray source observed during the interaction of a high intensity laser pulse with thin Au targets

A. Compant La Fontaine,¹ C. Courtois,¹ E. Lefebvre,¹ J. L. Bourgade,¹ O. Landoas,¹ K. Thorp,² and C. Stoeckl²

¹CEA, DAM, DIF, F-91297 Arpajon, France

²Laboratory for Laser Energetics, University of Rochester, Rochester, New York 14623, USA

(Received 1 October 2013; accepted 2 December 2013; published online 18 December 2013)

The interaction of a high intensity laser pulse on the preplasma of a high-Z solid target produced by the pulse's pedestal generates high-energy electrons. These electrons subsequently penetrate inside the solid target and produce bremsstrahlung photons, generating an x-ray source which can be used for photonuclear studies or to radiograph high area density objects. The source characteristics are compared for targets with thin (20 μm) and thick (100 μm) Au foils on the Omega EP laser at Laboratory for Laser Energetics. Simulations using the particle-in-cell code CALDER show that for a 20 μm thickness Au target, electrons perform multiple round-trips in the target under the effect of the laser ponderomotive potential and the target electrostatic potential. These relativistic electrons have random transverse displacements, with respect to the target normal, attributed to electrostatic fluctuation fields. As a result, the x-ray spot size is increased by a factor 2 for thin target compared to thick targets, in agreement with experimental results. In addition, the computed doses agree with the measured ones provided that electron recirculation in the thin target is taken into account. A dose increase by a factor 1.7 is then computed by allowing for recirculation. In the 100 μm target case, on the other hand, this effect is found to be negligible.

© 2013 AIP Publishing LLC. [<http://dx.doi.org/10.1063/1.4848759>]

I. INTRODUCTION

During the interaction of a high-intensity laser pulse produced by the chirped-pulse amplification (CPA) technique^{1,2} on the preplasma, usually formed in front of a solid target by the laser pulse's pedestal, relativistic electrons are produced by various physical processes.^{3,4} The one which mainly contributes, in the picosecond range laser pulse interacting onto a solid target, is the ponderomotive or $\mathbf{j} \times \mathbf{B}$ acceleration.^{5–7} These electrons subsequently collide with the atoms of the high-Z solid conversion target to produce a bremsstrahlung emission.^{8–11} This type of x-ray source thus formed find applications in various domains as for instance in radiography of dense objects,^{9,12–15} or photonuclear fission and activation studies.^{8,16,17} Their duration and spatial dimension are respectively in the picosecond and few hundred micron ranges, and the dose reaches up to several rads at 1 m in air.^{15,18} Dose optimization was previously studied versus different parameters, such as the preplasma length, the laser intensity or spot size, for a solid or a gas target or in a capillary filled with gas.¹⁹

The characteristics of an x-ray source (spot size, dose, and energy spectrum) are studied here both experimentally and numerically for thin Au targets (20 μm) compared to thick Au targets (100 μm). Experiments were performed on the Omega EP laser at the Laboratory for Laser Energetics²⁰ (LLE). Numerical simulations use the particle-in-cell (PIC) code CALDER⁸ to model the laser plasma interaction and the Monte Carlo N-particle transport code MCNP²¹ to compute the electrons collisions, including bremsstrahlung, in the target. The starting point of this study is the experimental

observation that the x-ray spot size is greater by about a factor of 2 for a 20 μm thickness Au target with respect to a 100 μm thickness Au target. Additionally, the dose measured experimentally for a 20 μm thickness Au target is found to be greater by about 70% than that expected by the simulation if one considers only a single passage of electrons across the target. On the other hand, the simulated dose is in agreement with the dose measured for a 100 μm thickness target. An element of answer to this problem is given by the effect of hot-electron recirculation in thin foils irradiated by ultraintense short laser pulse, already described in a number of publications.^{22–25} First, for a thin target, the electrons accelerated by the ponderomotive force are transmitted through the conductive target with little energy loss and merge at the backside of the target where they are reflected by the self-induced sheath electrostatic field. If the target thickness, x_t , is smaller than half the pulse length $c\Delta t_{\text{FWHM}}^{\text{laser}}/2$, where $\Delta t_{\text{FWHM}}^{\text{laser}}$ is the full width at half maximum (FWHM) pulse duration, the electrons returning from the rear can again be accelerated by the laser pulse, thus producing electron recirculation, which increases the effective electron density by the round trip number²³ $N = c\Delta t_{\text{FWHM}}^{\text{laser}}/(2x_t)$. Therefore, with $\Delta t_{\text{FWHM}}^{\text{laser}} = 0.6$ ps; for the 20 μm thickness target, electrons are expected to perform 4 round trips inside the target, while they experience only one transit for the 100 μm thickness target. However, simulations presented below show that the recirculation effect is active significantly longer than the laser pulse duration, but in a reduced section of the plasma. Electrons tracked are indeed reflected by the Debye sheath at both sides of the target. These Debye sheaths are generated by the electrostatic fields formed at both sides of the target

by the ejection of the target electrons when the bunch of the high energy electrons, accelerated by the ponderomotive force, passes through the target.

This simple model is checked by tracking test particles with CALDER through a $20\text{ }\mu\text{m}$ Au thickness target. The simulations confirm the recirculation effect of the electrons but with a number of electrons crossing the target, about twice smaller than expected by the model. In particular, electrons first accelerated by the laser pulse at a radius greater than the laser spot size $\phi_{\text{FWHM}}^{\text{laser}}$ do not recirculate in the target. Also, electrons exhibit transverse displacements attributed to electrostatic random fields.

The Omega EP laser facility is presented in Sec. II, with the diagnostics used, namely dosimeters, activation disks, and penumbral imaging to measure respectively dose, photon energy spectrum, and x-ray spot size. The CALDER simulations results, including the test particles analysis, are given in Sec. III. In Sec. IV, the experimental results, including the photon energy spectrum, the dose, and the x-ray spot size dimension are compared with the simulations, for the 20 and $100\text{ }\mu\text{m}$ thickness Au target cases. In addition, it is shown that for an Au target with thickness $x_t \sim 100\text{ }\mu\text{m}$, the mean electron distribution function (EDF) can be deduced from the experimental photon spectrum. The various results given in this article are summarized and discussed in Sec. V.

II. EXPERIMENT

The experiments are performed on the Omega EP laser at the University of Rochester LLE.²⁰ The diagnostics used here are presented in details in Ref. 26. The so-called “backlighter beam” is used in a high-intensity regime delivering up to 300 J in a 0.6 ps laser pulse of $1.054\text{ }\mu\text{m}$ wavelength. This backlighter beam is focused on target using an $f/2$ off-axis parabolic mirror, and 80% of the laser energy is contained within a $23\text{ }\mu\text{m}$ radius circle centered on the focal spot, so that the peak laser intensity is $4.4 \times 10^{19}\text{ W/cm}^2$. Targets are 20 and $100\text{ }\mu\text{m}$ thick, with respective transverse dimensions of 500×500 and $200 \times 200\text{ }\mu\text{m}^2$. The backlighter beam is linearly polarized and focused at the centre of the target front side, tilted by 45° relative to the laser beam axis to protect the off-axis parabolic mirror from potential target debris that are mainly produced perpendicularly to the target. The x-ray spectrum is inferred from photonuclear activation diagnostics and a hard x-ray spectrometer. The angular distribution of the x-ray dose is measured with series of optically stimulated luminescence (OSL) dosimeters placed at different ports behind aluminium flanges at various angular positions. A penumbral imaging diagnostic using a thick tantalum knife edge is used to measure the x-ray spot size.

III. ELECTRON TRANSPORT IN THIN AU TARGETS

The interaction of the laser with the preplasma formed by its pedestal in front of the Au target is modeled using the CALDER PIC code⁸ in two space dimensions (2D) in the (x,y) plane. The laser parameters used in the simulations are: energy in the focal spot $E_{\text{laser}} = 300\text{ J}$, laser spot size $\phi_{\text{FWHM}}^{\text{laser}} = 30\text{ }\mu\text{m}$, pulse duration $\Delta t_{\text{FWHM}}^{\text{laser}} = 0.6\text{ ps}$,

wavelength $\lambda = 1.053\text{ }\mu\text{m}$, p-polarization, and injection at 45° with respect to the target plane. The temporal and radial laser profiles are Gaussian. The maximal laser intensity is thus $I = 4.4 \times 10^{19}\text{ W/cm}^2$ and the peak normalized laser vector potential, $a_0 = eE_0/(m_e c \omega_0) = 2.70 \lambda[\mu\text{m}] \sqrt{I[10^{19}\text{ W/cm}^2]} = 5.69$, where e , m_e , c , E_0 , and ω_0 are, respectively, the electron charge and mass, the speed of light in vacuum, the laser electric field, and frequency. The mesh size is $\Delta x = \Delta y = \lambda/40$, and 20 macroparticles (electrons and ions) are used by cell to limit the numerical noise, so that the total kinetic energy gained by the plasma particles does not deviate from the total Poynting flux integral by more than a few per cent during the simulation. As 2D simulations can only compute linear particle densities, real particle numbers are obtained by multiplying these densities by a transverse dimension (along the missing z axis), equal to $1/2 \sqrt{\pi/\ln(2)} \phi_{\text{FWHM}}^{\text{laser}} = 32.59\text{ }\mu\text{m}$. This is obtained by equating the laser energy in 2D geometry (assuming invariance over this distance in the z direction), with the laser energy in 3D geometry, assuming a radial Gaussian intensity profile with similar spot size. The boundary conditions for the fields are periodic at the transverse boundaries and absorbing at the longitudinal boundaries; while for the particles, the boundaries are absorbing provided that the total electric charge in the domain remains null, otherwise particles are reinjected at thermal velocity in order to keep the total charge equal to zero. The characteristics of the accelerated relativistic electrons (position, velocity components, and weight of each macro-particle), first computed by CALDER, are then injected in the Monte Carlo code MCNP,²¹ using the proper target geometry, to model in 3D the electron-photon conversion process that takes place in the conversion target. A post-processor computes the angular distribution of the dose and the x-ray spot size, assuming cylindrical symmetry around the x axis in the target normal direction. The apparent x-ray source radial profile is obtained using a deconvolution method developed for similar studies on the AIRIX radiography machine.²⁷ The macro-particle number used in MCNP is adjusted to obtain statistical fluctuations of electron and photon data outputs within a few percents. For dose calculation, about 10^8 macro-particles are required; while for x-ray spot size calculation, more than 10^9 macro-particles are usually needed, representing about 10 to 150 h computing time on a standard monoprocessor PC workstation. Simulations with CALDER are performed using the Tera100 Bull supercomputer at CEA/DIF. The electron density of the preplasma formed by the laser pedestal is computed with the radiative hydrodynamic code CHIVAS.^{11,28} The laser contrast used in the simulation is the one measured on the multiterawatt (MTW) laser, prototype of Omega EP. It is equal to about 10^8 at 2 ns before the maximum intensity of the backlighter pulse. The electron plasma density profile, along the x axis, is often approximated by an exponential function, $n_e(x) = n_e(0) \exp(-x/L_p)$, with $x=0$ at the target surface plane, where the plasma scale length $L_p = 9\text{ }\mu\text{m}$ here. It is reported that the dose increases for long preplasmas, corresponding to large L_p values.¹¹ As the density gradient decreases, the laser energy absorption and the average kinetic energy of the

accelerated electrons increase, a behavior due to a transition from surface to volume absorption.²⁹

The recirculation of electrons in thin targets was already considered in proton acceleration studies, as this effect increases the energy of the ions accelerated in the Debye sheath at the rear of the target.^{22,23,30,31} In addition, the hot electron refluxing was found to increase the K-alpha emission for freestanding Cu foil targets.^{24,25} We study here the effects of the multiple crossing of electrons through thin targets on the x-ray source characteristics. CALDER simulations are done in a $(x,y) = 105 \times 180 \mu\text{m}$ simulation box with a $56 \mu\text{m}$ thick preplasma, with the above exponential density profile, starting at $4 \mu\text{m}$ from the left side with n_e increases from 1%, of is the critical density $n_c = m_e \epsilon_0 \omega_0^2 / e^2$, up to $5n_c$, followed by solid target modeled by a $20 \mu\text{m}$ thick plateau at $n_e/n_c = 5$ and with vacuum at the right of the target to let the electrons circulate, see Fig. 1(a). Electrons moving in

the domain under the effects of the electromagnetic and self-consistent electric and magnetic fields are selected when they cross a probe, represented by a red line in Fig. 1(a), from the inside to the outside. This probe is set in this simulation domain with its right edge at the back side of the target. The characteristics of these electrons then constitute the input data for the MCNP simulation; collisions are thus post-processed by MCNP. By noting that the various collisions encountered by the electrons in the target are not modeled in CALDER, the present method holds provided that the distance D covered by the electrons in the target is smaller than their diffusion depth x_D and range R in the target, given in Sec. IV A. This condition is fulfilled for instance for $N=4$ round trips made in the target, with thickness $x_t = 20 \mu\text{m}$, by the electrons with 2.6 MeV mean energies (see below), because $D = 2Nx_t = c\Delta t_{\text{FWHM}} = 180 \mu\text{m}$ is less than $x_D = 250 \mu\text{m}$ and $R = 660 \mu\text{m}$. In addition, after 4 round trips made in the

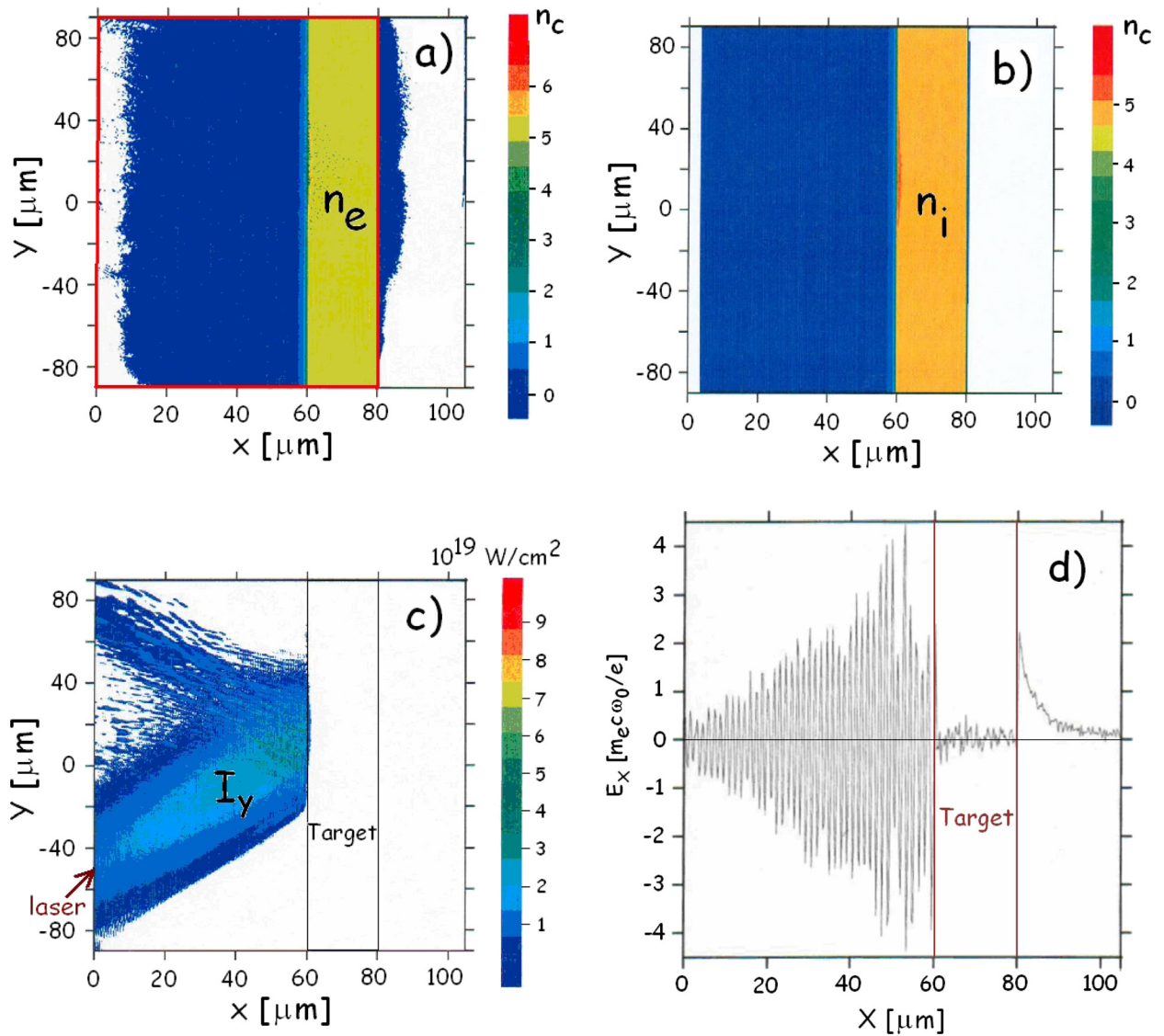


FIG. 1. Interaction of the laser pulse p polarized with maximal intensity $I = 4.4 \times 10^{19} \text{ W/cm}^2$ at 45° incidence at $x=0$, through a preplasma in front of a $20 \mu\text{m}$ thickness Au target at 0.88 ps when the laser peak intensity reaches the target. Initial conditions: preplasma from 4 to $60 \mu\text{m}$, with scale length $L_p = 8 \mu\text{m}$, target from 60 to $80 \mu\text{m}$ and vacuum elsewhere. (a) Electron density and probe (red line). (b) Ion density. (c) Laser intensity transverse component I_y . (d) Axial electric field E_x at $y=0$, along the x axis.

target, electrons with incident energies of 2.6 MeV and 10 MeV lose, respectively, about 30% and 13% of their energy by ionisation and bremsstrahlung, see Sec. IV A.

Thus, an electron passing through the target's back side and entering in the vacuum zone is added to the distribution each time it crosses a probe boundary (from inside to outside). This event may occur many times as it will be seen below. At 0.88 ps, when the laser peak intensity reaches its maximum on target, see Fig. 1(c), the head of the electron bunch accelerated by the ponderomotive force of the laser has already crossed the target and is situated at about $7 \mu\text{m}$ behind the target, see Fig. 1(a). At the same time, ions have not already moved, as it can be seen in Fig. 1(b), plotting the ion density. As a result, a Debye sheath forms at the back of the target. Its thickness is given by the Debye length λ_D given versus the density $n_{e,h}$, temperature T_h , and velocity v_{Th} of hot electrons: $\lambda_D = \frac{v_{Th}}{\omega_{pe}} \sqrt{\frac{kT_h}{4\pi e^2 n_{e,h}}} = 2.35 [\mu\text{m}]$

$\sqrt{T_h [\text{MeV}] / n_{e,h} [10^{19} \text{cm}^{-3}]}$, where ω_{pe} is the plasma frequency. In addition, in the laser intensity range 10^{18} to 10^{19}W/cm^2 , it was found by numerical simulations⁶ and experimentally⁵ that T_h could be approximated by the ponderomotive potential U_p : $T_h = U_p = m_e c^2 (\sqrt{1 + a_0^2} - 1)$, or by the Beg scaling³² $T_h = m_e c^2 a_0^{2/3}$ obtained from experimental results. On the other hand, Haines *et al.*³³ showed that these scaling do not longer hold at higher laser intensity and proposed the scaling: $T_h = m_e c^2 (\sqrt{1 + \sqrt{2} a_0} - 1)$, obtained with a relativistic model based on energy and momentum conservation laws of the laser interaction with an overdense plasma. This scaling is in agreement with experimental results and with recent 3D PIC simulations³⁴ in the 10^{18} to 10^{20}W/cm^2 laser intensity range. In a fully relativistic regime, $v_{Th} = c$ and $\omega_{pe} = \omega_0 \sqrt{\frac{n_{e,h}}{\gamma n_c}}$, where $\gamma = 1 + a_0/\sqrt{2}$ is

the relativistic factor, so that $\lambda_D = \frac{\lambda}{2\pi} \sqrt{\frac{(1+a_0/\sqrt{2})n_c}{n_{e,h}}}$. The electrostatic field E_x in the Debye sheath $E_x = \sqrt{2} T_h / (e \lambda_D)$ is obtained by Carron *et al.*³⁵ by solving the Boltzmann equation with a potential derived by solving the Poisson equation for the following EDF: $dN_e/dE = N_0/T_h^2 \exp(-E/T_h)$; thus, $E_x = E_0 \sqrt{\frac{n_{e,h}/n_c}{1+a_0/\sqrt{2}}}$. The field E_x plotted in Fig. 1(d) on the axis ($y=0$) has two contributions: the incident oscillating electric field of the laser pulse at the left of the target and the electrostatic field E_x in the Debye sheaths at both edges of the target. For the present experiment, numerical simulations and theory in fully relativistic regime give, respectively: $T_h = 1.7$ and 2.0 MeV , $n_{e,h} = 7.0 \times 10^{21}$ and $5.9 \times 10^{21} \text{ cm}^{-3}$, $\lambda_D = 0.12$ and $0.14 \mu\text{m}$, and at the right side of the target, $E_x = 7.0$ and 8.1 TV/m (with $m_e c \omega_0 / e = 3.21 \text{ TV/m}$).

Note that the electrostatic field is clearly seen behind the target, but is hardly noticeable in front of the target due to the contribution of the oscillating laser electric field component. In addition, the bunch of high energy electrons accelerated by the ponderomotive force sets up a large electrostatic field: $|\vec{E}(a)| = I / (2\pi \epsilon_0 a c \beta)$, where I is its intensity, a its

radius, and $\beta = v_{Th}/c$. The electron bunch duration is about 1.5 ps (or $2.5 \times \Delta t_{FWHM}^{\text{laser}}$). By crossing the target, electrons of the target are expelled so that the target gets positively charged (effect observed in the simulation), thus producing electrostatic fields at both sides of the target, which remain after the end of the laser pulse. As a result, the recirculation effect of the electrons reflected by the Debye sheaths at both sides of the target is expected to take place during a time longer than the laser pulse duration.

Test macroparticles (electrons) are selected in CALDER, provided that they cross the back side of the target ($x = 80 \mu\text{m}$) at a radius smaller than $50 \mu\text{m}$ and with an energy greater than 1 MeV (in order to select non-thermal electrons). These test electrons (which likely gained their energy from the ponderomotive force) are then tracked until they leave the simulation domain. A total of 120 such test macroparticles are randomly selected, but less than 50 of them do at least one round trip in the target from the beginning of their track, with initial radius smaller or equal to $30 \mu\text{m}$, while the remaining 70 test macroparticles do not recirculate in the target. The test macroparticle (electron) #26 tracked from $(x,y) \sim (80, 0) \mu\text{m}$, represented in Fig. 2(a), exhibits 6 round trips before it returns to the preplasma where its trajectory is driven by the random fields before it is lost at the upper side of the simulation box at $y = 90 \mu\text{m}$. The axial x position time evolution of a few test macroparticles, plotted in Fig. 2(b), shows 6 round trips for 3 of them (#10, #26, and #29) with initial transverse position $y_0 = 0$, and no round trip for 2 of them (#33 and #35) with $y_0 = 30 \mu\text{m}$. This result indicates that at radius greater than $\phi_{FWHM}^{\text{laser}}$, the laser field and the sheaths electrostatic fields are not large enough to accelerate electrons sufficiently to make them cross the target. Note also that the value of 6 round trips made by these first three test particles is greater than that of $c\Delta t/(2x_t) = 4$ given by the model of Reference 23: indeed, these test macroparticles cross the target at instants until $\sim 1 \text{ ps}$ after the end of the laser pulse. The axial momenta of the two test macroparticles #10 and #26 (drawn respectively with blue and red lines in Fig. 2(b)) are represented versus time in Fig. 2(c). The minimum and maximum momenta have about the same absolute value, because the axial laser electric field component is about equal to the axial electrostatic field, as seen above. In addition, the recirculating test macroparticles #10, #26, and #29 have initial energies, respectively, equal to 3.5, 1.5, and 2.3 MeV, which increase up to maximum values of 22, 19, and 10 MeV, and have 9, 15, and 7 MeV at the final round trip. Thus, as it will be confirmed below, the EDF for the $20 \mu\text{m}$ thickness target is expected to be substantially modified with respect to the case of a thicker target, where the recirculation of electrons does not take place. Another feature of the test macroparticles is their transverse displacement given by the co-ordinate y , which is found to vary randomly up and down versus time, under the effect of the random electric fields, see Fig. 2(d), some of the macroparticles even reaching the upper or lower limit of the simulation box at $y = \pm 90 \mu\text{m}$. This will lead to an increase of the target electron spot size, and one can also expect an increase of the x-ray spot size, a result confirmed below in Sec. IV C.

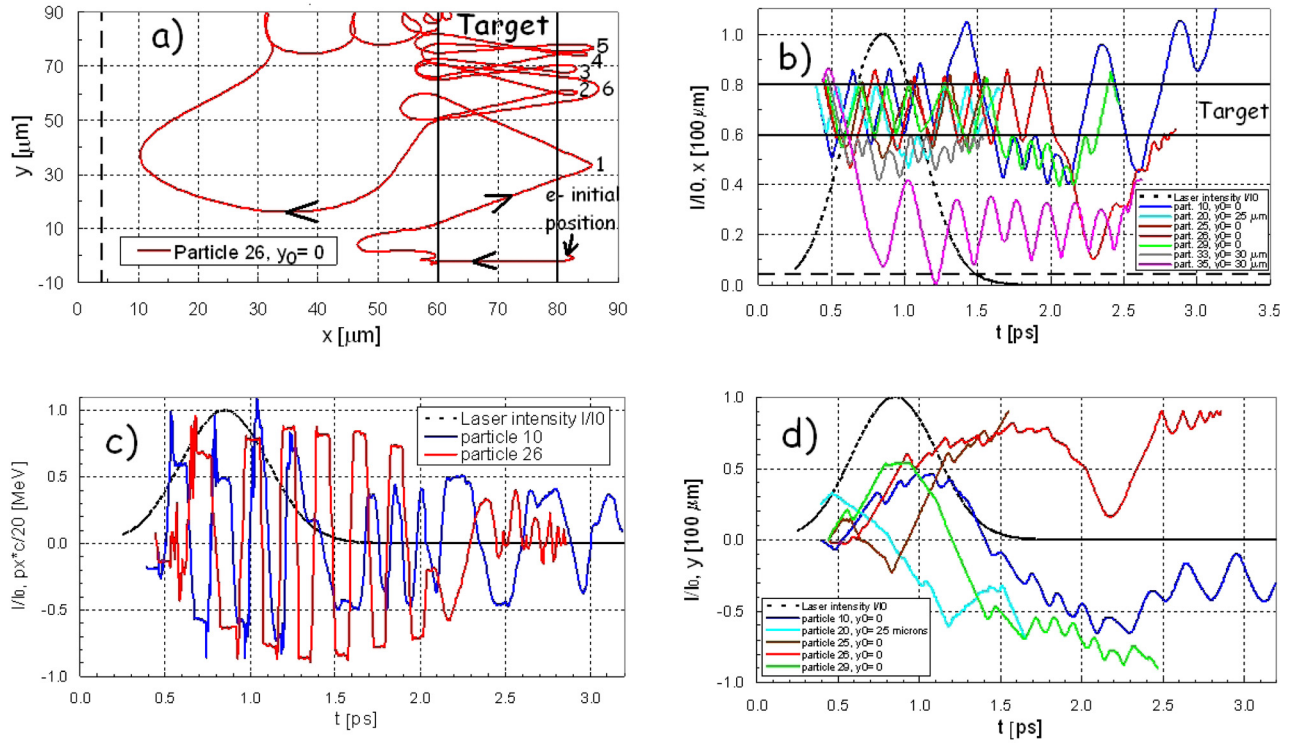


FIG. 2. Electron test particles tracked with CALDER. (a) Trajectory in (x,y) coordinates of particle #26 (solid red line) with initial transverse positions: $y_0 = 0$, and initial preplasma (dashed line) and target (solid line) limits, and round trip number. (b) Axial positions of several test particles versus time tracked from different initial transverse positions: $y_0 = 0$ (blue, brown, red, and green lines), $y_0 = 25 \mu\text{m}$ (light blue), and $y_0 = 30 \mu\text{m}$ (grey and pink lines). The normalized laser intensity at the target left side position is represented in dotted line. (c) Axial momenta of two test particles #10 and #26 at $y_0 = 0$ (red and blue lines), versus time. (d) Transverse position of circulating test particles of Fig. 2(b) given versus time.

In order to compare cases with and without electron recirculation in the target, another CALDER simulation is done for the $100 \mu\text{m}$ target thickness case by simply running the previous simulation without vacuum at the right of the target, in order to inhibit electronic recirculation in the target. The normalized total electron energy at each angle corresponding to the electrons crossing the right side of the probe box as computed by CALDER for the cases with 20 and $100 \mu\text{m}$ thickness Au targets (i.e., respectively with and without electron recirculation in the target) is represented in Fig. 3(a). The angular extent of the electron angle-dependant energy distribution is slightly greater for the $20 \mu\text{m}$ thickness target than for the $100 \mu\text{m}$ case, which are, respectively, $\theta_{\text{FWHM}} = 116^\circ$ and 101° . This result is attributed to two

reasons linked to electron recirculation in the target: the first one is due to the transverse displacement of the recirculating electrons that induce angular broadening of the electron emission, and the second one results from the increase of the electron energy during the recirculation process. Indeed, it can be seen on the EDF plotted in Fig. 3(b) for the two target thickness cases at 100 and $20 \mu\text{m}$, that there is an energy transfer of electrons from low to high energy, which is attributed to the recirculation process in the $20 \mu\text{m}$ case. The low part of the EDF ($E < 0.3 \text{ MeV}$) is flatter for the $20 \mu\text{m}$ case than for the $100 \mu\text{m}$ case, because for the $20 \mu\text{m}$ case electrons with energy $E \ll U_p = 2.4 \text{ MeV}$ and merging at the backside of the target are slowed down more efficiently than the higher energy ones by the electrostatic sheath at the

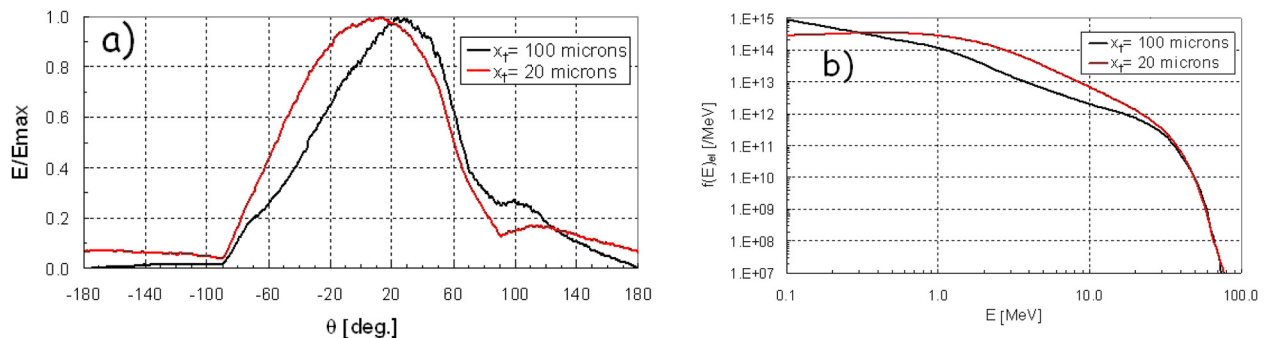


FIG. 3. (a) Normalized total angular electron energy distribution calculated by CALDER for the cases without and with electron recirculation for target thickness x_t of respectively 100 and $20 \mu\text{m}$ thicknesses. (b) Angularly integrated energy distribution functions in the forward direction of the incident electrons for the targets of the two previous cases.

backside of the target, which one is absent in the 100 μm case. As a result, the mean electron energy for the 100 and 20 μm thick targets cases are, respectively, equal to 1.8 and 2.6 MeV. Moreover, at small target thickness (20 μm), the electron recirculation effect produces an increase of the number of electrons crossing the target with energy comprised between about 0.2 to 40 MeV. At high energy ($E > 40$ MeV), electrons escape from the Debye sheaths and do not recirculate. In addition, electrons accelerated early during the laser pulse have less energy than those accelerated later because as the laser intensity increases until it reaches its maximum at 0.8 ps. Once these electrons have passed the back of the target, they can return to the target under the effect of the Debye sheath. Then, the laser intensity they encounter is greater and they are heated more efficiently by the ponderomotive force (see remark above). This is the case for instance of the macroparticle #26, which has a relatively small axial momentum when it merges at the back of the target during the rising front of the laser pulse at 0.55 ps, and later in time at 0.7 ps at the next round trip, its momentum is noticeably increased, see Fig. 2(c). Thus, the total number of electrons, with energy greater than 50 keV, crossing the target is, respectively, equal to 4.1 and 8.6×10^{14} for the 100 and 20 μm thicknesses Au targets, respectively, without and with electron recirculation. Thus, the recirculation effect contributes to increase by about only a factor 2, the number of electrons crossing the target, that is twice less than the factor 4 expected by the model of Sentoku *et al.*²³ Indeed, among the 120 macroparticles tracked in the simulation, a total of 175 round trips are observed and 70 of them, mostly starting at radii greater than $\phi_{\text{FWHM}}^{\text{laser}}$, cross the target only once.

IV. X-SOURCE CHARACTERISTICS

The experimental results of the photon energy distribution function, dose, and x-ray spot size are compared here with the simulation for the 20 and 100 μm thickness Au targets, respectively, with and without electron recirculation. Moreover, the contribution of the recirculation effect of electrons in the target is quantified.

A. X-ray spectrum

The energy distribution of photons produced in the Au conversion targets is obtained experimentally with an

activation diagnostic and a hard x-spectrometer.²⁶ The activation measurements are based on $^{63}\text{Cu}(\gamma, n)^{62}\text{Cu}$ and $^{12}\text{C}(\gamma, n)^{11}\text{C}$ photo-nuclear reactions. The hard x-ray spectrometer uses a number of optically stimulated luminescent (OSL) dosimeters sandwiched between high Z filters housed inside a tungsten collimator.

The experimental photon energy distribution function $f_{\text{ph}}(k)$ is fitted with the analytical expression: $f_{\text{ph}}(k) = \frac{dN_{\text{ph}}}{dk} = K[(1 - b + \frac{T}{k})e^{-\frac{k}{T}} + (b - \frac{E_0}{k} - \frac{T}{k})e^{-\frac{E_0}{T}}]$ versus the photon energy k , where $b \cong 0.83$ and E_0 is the high-energy cut-off^{36,37} ($E_0 = 50$ MeV here) with two adjustable parameters K and T . The x-ray spectrum is then reconstructed by matching calculated results obtained by convolving the x-ray spectrum with the spectral responses of the hard x-ray spectrometer and activation measurement (photo-nuclear reaction cross sections), with the corresponding experimental results from these two diagnostics. The photon energy distribution function $f_{\text{ph}}(k)$ is given for the 100 and 20 μm thickness Au targets respectively in Figs. 4(a) and 4(b). The coloured zones correspond to various values of K and T giving an agreement between the previous expression and the experimental results. The simulations and experimental results are compatible within the experimental uncertainty range. The contribution of the electron recirculation in the 20 μm thickness Au target of Fig. 4(b) (solid line) increases the photon emission by about a factor of two below 4 MeV and makes no change above 10 MeV, if one no consider electron recirculation (dotted line). This effect is however too small to be checked experimentally with respect to the experimental uncertainties. Note that the experimental and numerical photon spectrums are very similar to the EDF obtained on K-alpha sources.²⁵

In the following, we study the possibility to infer the EDF from the experimental photon spectrum. This topic was already discussed in a previous paper, but not addressed fully.²⁴ The EDF produced during the laser plasma interaction is usually measured using an electron spectrometer.¹³ However, if one wants to measure the EDF in the direction of the laser axis, one need to use thin targets in order to prevent electrons from being deflected and absorbed in the target, respectively, by elastic and inelastic collisions. On the other hand, electrons with energy much smaller than the ponderomotive potential are retained by the Debye sheath at the back of the target and thus do not reach the spectrometer,

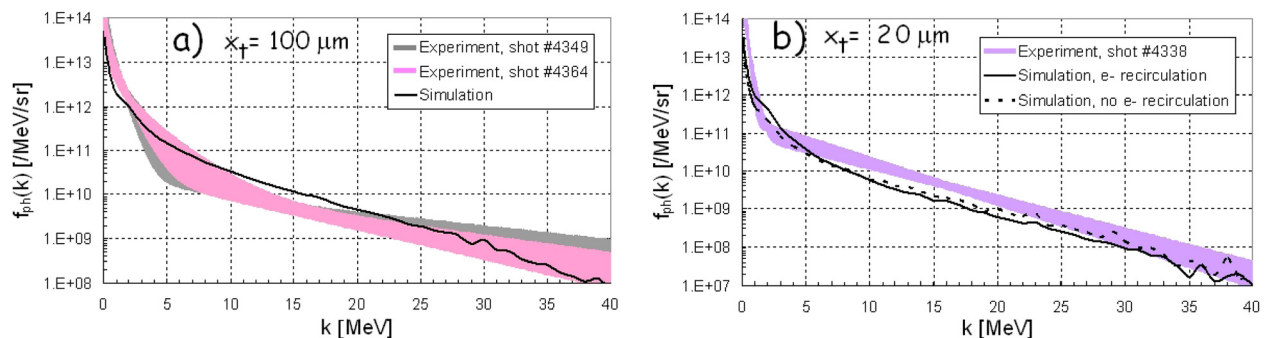


FIG. 4. (a) Energy distributions functions of hard x-ray emission behind Au targets, with thickness x_t of (a) 100 μm and (b) 20 μm . The contribution of recirculating electrons is represented in dotted line for the case (b).

which underestimates the EDF at low energy. In order to overcome this problem, the EDF can be alternately deduced by deconvolving the x-ray spectrum. The photon spectrum can be measured by various diagnostics as thermoluminescent dosimeters,³⁸ hard x-ray spectrometer,^{26,38} activation diagnostics,^{11,15–17,26} or bremsstrahlung spectrometer.³⁹ The conditions to infer the EDF from the experimental photon distribution function is first to assume that the EDF is isotropic and secondly the target thickness must be sufficiently small so that the deflections and energy loss of the electrons in the target are negligible, as well as other processes such as photon absorption. The mean angular photon energy spectrum dN_{ph}/dk can then be obtained by integration of the EDF over the intergrated-over angle bremsstrahlung cross section:⁴⁰ $d\sigma/dk = aZ^2(1/k - b/E)$, with $a \cong 11$ mb and $b \cong 0.83$: $\frac{dN_{ph}}{dk} = n_a x_t \int_k^{E_m} \frac{d\sigma}{dk} f_{el}(E) dE = f_{ph}(k)$, where n_a is the atomic density and $f_{el}(E)$ the EDF.³⁶ The EDF given by CALDER simulations, obtained from the interaction of a high intensity laser with a preplasma in front of a solid target, may generally be interpolated by a sum of two exponentials, as: $f_{el}(E) = K_1 \exp(-E/T_1) + K_2 \exp(-E/T_2)$, where K_1 , K_2 , T_1 , and T_2 are adjustable constants. The photon distribution function then writes versus the photon energy k

$$\frac{dN_{ph}}{dk} = n_a e a Z^2 \left\{ \frac{1}{k} \left[-T_1 k_1 (e^{-E_m/T_1} - e^{-k/T_1}) - T_2 k_2 (e^{-E_m/T_2} - e^{-k/T_2}) \right] - b \left[k_1 \left(E_1 \left(\frac{k}{T_1} \right) - E_1 \left(\frac{E_m}{T_1} \right) \right) + k_2 \left(E_1 \left(\frac{k}{T_2} \right) - E_1 \left(\frac{E_m}{T_2} \right) \right) \right] \right\},$$

where E_1 is the exponential integral function.⁴¹ The incident EDF, given by CALDER, is represented in Fig. 5(a) with its interpolation function $f_{el}^{fit}(E)$ given in units /MeV/sr with $K_1 = 5.43 \times 10^{13}$ photons/MeV/sr, $K_2 = 1.04 \times 10^{12}$ photons/MeV/sr, $T_1 = 0.901$ MeV and $T_2 = 9.01$ MeV, and the transmitted EDF, calculated with MCNP, through a 100 μ m thickness Au target. Below about 1 MeV, electrons lose their energy by ionisation in the matter and the fraction of electrons transmitted significantly reduces (at 1 MeV, the ionisation range in Au is about 250 μ m). The on-axis photon spectrum $f_{ph}(k)$ [MeV/sr] given by the above analytical expression is compared in Fig. 5(b) with the MCNP simulation for $f_{el}^{fit}(E)$ chosen isotropic, for a 100 μ m thickness Au target, and the two curves show deviations smaller than a factor 2 in the 0.1 to 80 MeV energy range. The model is then tested for different target thicknesses with MCNP simulations also for an isotropic EDF with the above parameters K_1 , K_2 , T_1 , and T_2 . Fig. 5(c) plots the on-axis ratio of the photon number given by the model to that obtained by the MCNP simulation, by integration of $f_{ph}(k)$ in the 0.1 to 80 MeV energy range. Note that off-axis photon spectrum (not represented here) differs from that on-axis, because the length crossed by the electrons in the target is greater at oblique direction; its level is thus higher at small target thickness and smaller at higher target thickness as it reaches the photon absorption length in matter (due to

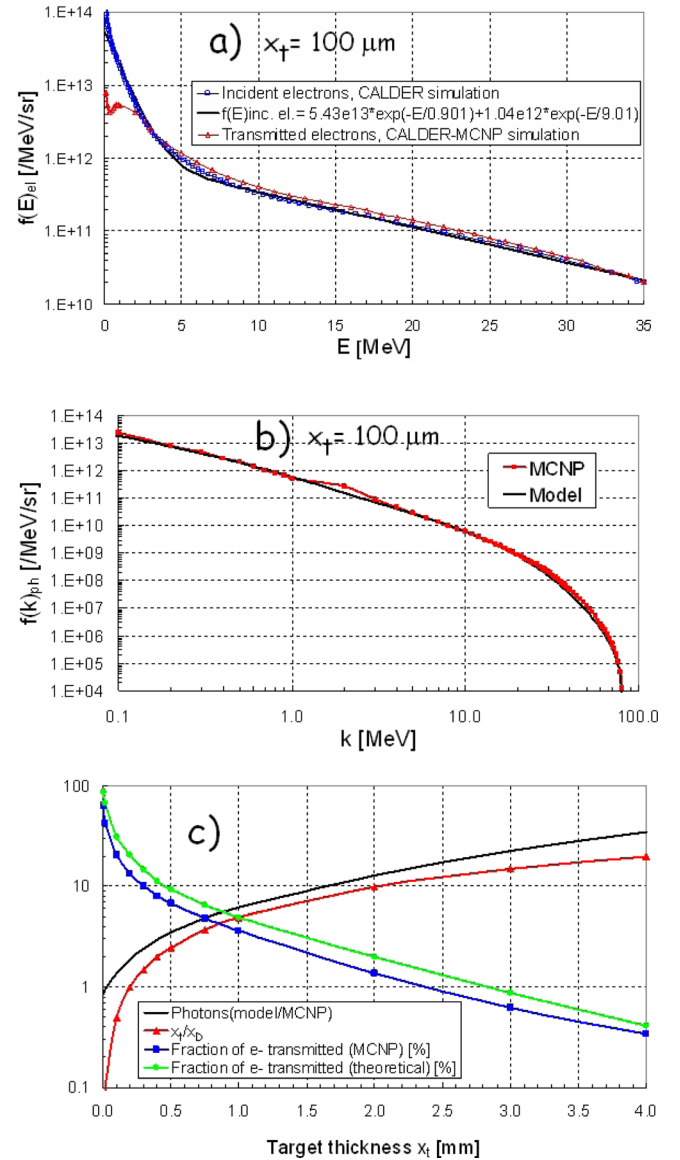


FIG. 5. (a) Energy distributions functions of incident electrons (blue line) on a 100 μ m thickness Au target given by CALDER without electron recirculation, fitted with a sum of two exponentials (black line) and transmitted electrons (red line) obtained by MCNP. (b) On-axis photon energy spectrum obtained by MCNP simulation with incident EDF given by the previous fit and chosen isotropic (red line) and photon energy spectrum given by the model (black line). (c) Ratio of the photon numbers given by the model to that obtained by MCNP simulations (black line), versus target thickness, for an isotropic incident EDF given by the interpolation function of Fig. 5(a), with integration of the photon emission spectrum between 0.1 and 80 MeV; fraction of the electrons transmitted to that incident computed by MCNP (blue squares) together with the Kanaya *et al.*³⁸ theoretical expression (green dots); and ratio of the target thickness x_t to the electron diffusion depth x_D (red triangles).

coherent-Rayleigh and incoherent-Compton diffusion, photoelectric effect, and electron-positron pair creation). At the smallest target thickness simulated (5 μ m), the model underestimates the photon production by about 15%. On the other hand, for x_t greater than the diffusion depth x_D of electrons in the target, the fraction of electrons transmitted η_T to that incident obtained by MCNP falls below 15%, see Fig. 5(c), and the model ceases to be valid. The diffusion depth is expressed by Kanaya *et al.*⁴² $x_D = R/(1 + \gamma)$, where the

range R or energy loss by ionisation is given by Katz and Penfold⁴³ $R = (0.530E - 0.106)/\rho$ in cm, with the electron energy E in MeV and the target density ρ in g/cm³, and with $\gamma = 0.187Z^{2/3}$ for $E < 1$ MeV and $\gamma = 0.22Z/\ln(ZE/0.0135)$ for $E > 1$ MeV, where Z is the atomic number of the target. Note that the fraction of electrons transmitted given by the theoretical model⁴² $\eta_T = \exp[-\gamma y/(1-y)]$, with $y = x/R$, is overestimated by about 50%. The main contribution of the relative energy loss by an electron in a solid target is due to ionisation, which writes at distance x in the target⁴² $\Delta E/E = (1-y)^{3/5} - 1$, so that the electron loses 1/e of its energy by ionisation at length $l_i = (1 - e^{-5/3})R$. Other contribution to the electron energy loss is caused by the bremsstrahlung emission in the field of the atom (nucleus and atomic electrons), which is expressed by the radiation length in relativistic regime in the case of complete screening⁴⁴ $l_R = \frac{716.4A}{\rho Z(Z+1)\ln(183Z^{-1/3} + 1/18)}$, distance along with the electron loses 1/e of its energy, where A is the target atomic mass and ρ is in g/cm³. Note that for a 2.6 MeV mean electron energy of the EDF, $l_R/l_i \sim 5$, so that the energy loss by bremsstrahlung represents about 20% of the energy loss by ionisation, where the total electron energy loss is given by $dE/E = -dx(1/l_R + 1/l_i)$. In addition, as seen above, target thickness must be greater than half the pulse length in order to prevent electron recirculation in the target to occur, otherwise the photon spectrum level would be modified, as seen above, and the incident EDF deduced would be erroneous. Thus, if the target thickness chosen fulfils the condition: $c\Delta t_{FWHM}^{laser}/2 < x_t < x_D$, the incident EDF $f_{el}(E)$, can be deduced from the experimental photon spectrum, provided that $f_{el}(E)$ is isotropic. For instance, in the present experimental conditions, the optimal Au target thickness would be $x_t \sim 100 \mu\text{m}$ for which the relative total electron energy loss in the target is $\Delta E/E \sim 20\%$.

B. Dose

We now try now to quantify the effect on dose of the electron recirculation in the thin target. Dose is measured by OSL dosimeters behind aluminium flanges, which are modeled in the MCNP simulations. The energy response of the OSL dosimeters is: 5 keV to 40 MeV, see Ref. 45. The minimum energy considered in the CALDER and MCNP simulations is equal to the photon energy cut-off of the aluminium flanges, i.e., 50 keV. Dose given at 1 m in air is integrated from 50 keV to 80 MeV, which corresponds to the maximum energy of electrons obtained in the CALDER simulations. In addition, the simulations show that the dose integrated versus the energy saturates at about 30 MeV. The ratio of dose measured on the $x_{t1} = 20 \mu\text{m}$ to the $x_{t2} = 100 \mu\text{m}$ thicknesses Au targets is equal to: $f_{1,2}^{\text{exp}} = 0.54 \pm 15\%$. Note that the relatively small fluctuations at 8% of dose measurements obtained at different angular positions for a few shots can be attributed to the large laser spot size ($\phi_{FWHM}^{laser} = 30 \mu\text{m}$), which is expected to reduce the laser-plasma bifurcation instability.¹⁹ The rectangular targets with 20 and 100 μm thicknesses with respective transverse dimensions 500×500 and $200 \times 200 \mu\text{m}^2$ are equivalent to circular targets with same surfaces with respective radii of $r_1 = 280$ and

$r_2 = 110 \mu\text{m}$. The contribution of recirculating electrons to dose then writes: $f_R^{\text{exp}} = f_{1,2}^{\text{exp}} \cdot g_{2,1} \cdot h_{2,1}$, where $g_{2,1}$ is the dose ratio for a 100 to a 20 μm thicknesses Au target with the same radius and without electron recirculation in both cases, and $h_{2,1}$ is the dose ratio for a 110 to a 280 μm radius Au targets. Using MCNP, we obtain: $g_{2,1} = 3.3$ and $h_{2,1} = 0.94$, thus we have: $f_R^{\text{exp}} = 1.7\% \pm 15\%$. The on-axis dose is obtained by injecting a high macroparticle number in MCNP (up to 6×10^9) to reduce the relative error. The previous result, obtained by using 6 different CALDER simulations done with and without electron recirculation and by varying the simulation domain size, gives with MCNP on-axis dose fluctuations of about 15%. In addition, by using CALDER simulation results with and without electron recirculation (with respectively vacuum and no vacuum behind the target), we obtain by running MCNP the same result as that given by the experiment within experimental and numerical fluctuations, i.e., $f_R^{\text{sim}} \cong f_R^{\text{exp}} \cong 1.7\% \pm 15\%$. Note that as this ratio drops the uncertainty of absolute dose calibration measurements as well as absolute dose values obtained in the simulations, it is thus simply directly related to the electron recirculation effect. In addition, this ratio 1.7 is smaller than the factor 4 expected by the model of Ref. 23. As expected, the dose increase factor of 1.7 induced by electron recirculation is between the factors 1.5 and 2, which correspond to the ratios of the mean electron energies and the electron numbers of the EDF of the 20 and 100 μm Au target thicknesses, respectively.

C. X-ray spot size

The x-ray source spot size is measured experimentally, for shots 4337 and 4336 with, respectively, 100 and 20 μm thicknesses Au targets from a penumbral imaging diagnostic using tantalum knife edge placed at 250 mm from the source.¹⁵ The penumbral image of the x-ray source is recorded with image plates⁴⁶ (IP) placed at 3650 mm from the knife edge, which gives a magnification of the image equal to 14.6. A 230 μm thick tantalum screen is positioned in front of the image plate to reinforce the signal by converting part of the x-ray photon energy into Compton electrons that have better energy deposition within the IP. The spatial profiles of the photo stimulated luminescent (PSL) records obtained on the IP are given in Figs. 6(a) and 6(b), respectively, for the 100 and 20 μm thick targets. These profiles are interpolated with an edge response function (ERF) associated here to an x-ray source with a Bennett radial profile, $f_B(r) = [1 + (r/a_2)^2]^{-2}$, characterized by a width a_2 that can be related to the full width at half maximum by: $FWHM = 2(2^{1/2} - 1)^{1/2} a_2$. The Bennett fit gives source sizes for the 100 and 20 μm thicknesses Au targets of, respectively, $\phi_{FWHM}^x = 87 \pm 30 \mu\text{m}$ and $156 \pm 40 \mu\text{m}$. The size uncertainty is due to the knife edge and detector resolution.

The penumbral image is simulated with MCNP, by using the CALDER results. The knife edge geometry is modelled in MCNP, as the tantalum screen in front of the image plate. The blur image is simulated by considering the total photon energy incident on each pixel at the image plate position. It is necessary to use about 2×10^9 input sampling electrons in MCNP to obtain sufficient statistics in the signal

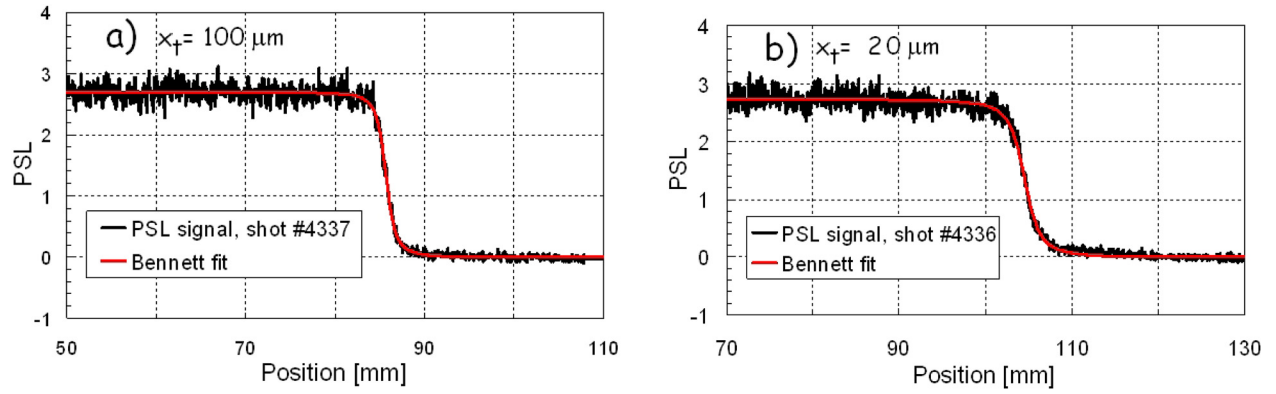


FIG. 6. (a) and (b) Measured spatial profiles, in PSL scale, of the penumbral images obtained by the image plates for shots nos. 4337 and 4336 with Au target thicknesses x_t of respectively 100 and 20 μm , with Bennett fit (red line).

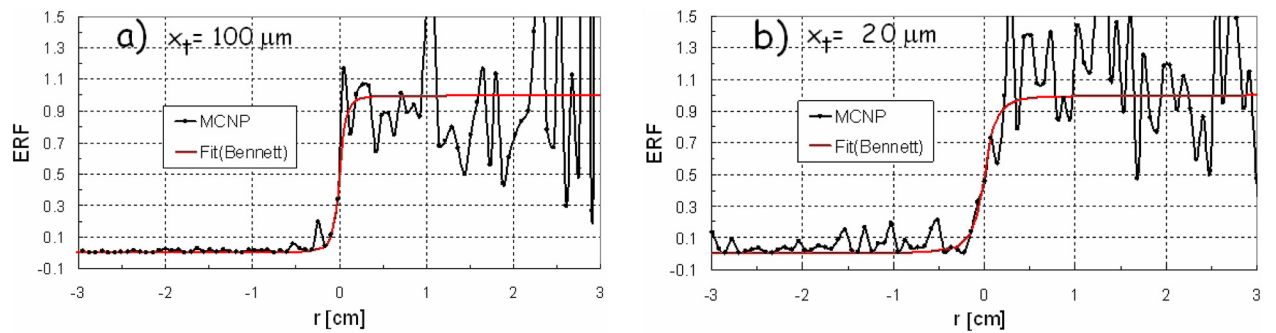


FIG. 7. (a) and (b) Calculated spatial profiles of the ERFs of the penumbral images for the targets with respectively the 100 and 20 μm thicknesses x_t simulated with CALDER and MCNP behind the knife edge, with Bennett fit (red line).

in order to extract an interpolated response curve. The signal-to-noise ratio may be improved by increasing the number of macroparticles in the PIC simulation, but this would increase the running time. The ERFs thus obtained by the MCNP simulations for the 100 and 20 μm thickness Au targets are represented, respectively, in Figs. 7(a) and 7(b). The spot size is obtained by the LANL-CEA/VM reference method, which consists in making the deconvolution of the response curve to get the x-source radial profile.²⁷ The x-source radial profile obtained is Bennett-type, which is a common characteristic of bremsstrahlung sources derived from thick target converters.^{11,15,19,27} For the 100 and 20 μm thickness Au targets, the x-ray spot sizes full width at half maximum are, respectively, equal to $\phi_{\text{FWHM}}^x = 65$ and 126 μm . The x-ray spot size corresponding to the 20 μm thickness target is thus about twice that of the 100 μm thickness target, close to the experimental results. The x-ray spot size increases for a 20 μm thick target, with respect to a 100 μm thick target, because of random transverse drifts that the electrons execute as they operate multiple passages in the target, which also induces an increase of the angular electron energy lobe width, as seen in Sec. III. This is in agreement with a previous result that showed that the x-ray spot size is close to the electron spot size at the target.²⁷

V. CONCLUSION

Experiments Au targets of various thicknesses (20 and 100 μm) done on the Omega EP laser at LLE give rise to the

study of the electron recirculation process in high intensity laser matter interaction experiments. Using the PIC code CALDER, test electron particles leaving the 20 μm thickness Au target with energy greater than 1 MeV are followed until they leave the simulation domain, well after the laser pulse ends. Electrons generated inside a radius smaller than the laser spot size ϕ_{FWHM} recirculate inside the target confined by the ponderomotive potential of the laser and the electrostatic potential. Moreover, the recirculation process can last during a time longer than the laser pulse duration, under the effect of Debye sheaths that develop at both sides of the target. The Debye sheath is formed when the relativistic electrons produced by the ponderomotive force exit at the back of the target, and expel electrons of the target. In addition, the electrons move randomly along their trajectory in the transverse direction under the effect of random fields. Simulations show that, under the effect of the recirculation process, the number of electrons crossing the 20 μm thickness target increases by a factor of about 2, which is less than the value of 4 predicted by the model of Sentoku *et al.*²³ As a result, the recirculation process increases dose by a factor of 1.7, as found experimentally and by the simulation, using the Monte Carlo code MCNP, which computes the bremsstrahlung process in the solid target. In addition, the x-ray spectra obtained experimentally agree with simulation results, within experimental uncertainties. The increase by about a factor 2 of the x-ray spot size, obtained experimentally and by the simulation, is the result of the random

transverse displacement operated by the electrons during their multiple crossings through the target. An interesting diagnostic tool of the incident EDF (assumed isotropic) on the target, deduced by using the experimental on-axis x-ray spectrum is demonstrated here by using MCNP; it is found that this method can be used for target thicknesses greater than the laser half pulse width and smaller than the electron diffusion path.

ACKNOWLEDGMENTS

We acknowledge the support of the engineering/target area and target preparation staff of the Omega EP laser facility.

- ¹G. Malka, M. M. Aléonard, J. F. Chemin, G. Claverie, M. R. Harston, J. N. Scheurer, V. Tikhonchuk, S. Fritzler, V. Malka, P. Balcou, G. Grillon, S. Moustazis, L. Notebaert, E. Lefebvre, and N. Cochet, *Phys. Rev. E* **66**, 066402 (2002).
- ²M. Gerbaux, F. Gobet, M. M. Aléonard, F. Hannachi, G. Malka, J. N. Scheurer, M. Tarisien, G. Claverie, V. Méot, P. Morel, J. Faure, Y. Glinec, A. Guemnie-Tafo, V. Malka, M. Manclossi, and J. J. Santos, *Rev. Sci. Instrum.* **79**, 023504 (2008).
- ³A. Pukhov, *Rep. Prog. Phys.* **66**, 47 (2003).
- ⁴M. I. K. Santala, M. Zepf, I. Watts, F. N. Beg, E. Clark, M. Tatarakis, K. Krushelnick, A. E. Dangor, T. McCanny, I. Spencer, R. P. Singhal, K. W. D. Ledingham, S. C. Wilks, A. C. Machacek, J. S. Wark, R. Allot, R. J. Clarke, and P. A. Norreys, *Phys. Rev. Lett.* **84**, 1459 (2000).
- ⁵G. Malka and J. L. Miquel, *Phys. Rev. Lett.* **77**, 75 (1996).
- ⁶S. C. Wilks, W. L. Kruer, M. Tabak, and A. B. Langdon, *Phys. Rev. Lett.* **69**, 1383 (1992).
- ⁷A. Pukhov and J. Meyer-ter-Vehn, *Phys. Plasmas* **5**, 1880 (1998).
- ⁸E. Lefebvre, N. Cochet, S. Fritzler, V. Malka, M. M. Aléonard, J. F. Chemin, S. Darbon, L. Disdier, J. Faure, A. Fedotoff, O. Landoas, G. Malka, V. Méot, P. Morel, M. Rabec Le Gloahec, A. Rouyer, Ch. Rubbelynck, V. Tikhonchuk, R. Wrobel, P. Audebert, and C. Rousseaux, *Nucl. Fusion* **43**, 629 (2003).
- ⁹R. D. Edwards, M. A. Sinclair, T. J. Goldsack, K. Krushelnick, F. N. Beg, E. L. Clark, A. E. Dangor, Z. Najmudin, M. Tatarakis, B. Walton, M. Zepf, K. W. D. Ledingham, I. Spencer, P. A. Norreys, R. J. Clarke, R. Kodama, Y. Toyama, and M. Tampo, *Appl. Phys. Lett.* **80**, 2129 (2002).
- ¹⁰P. A. Norreys, M. Santala, E. Clark, M. Zepf, I. Watts, F. N. Beg, K. Krushelnick, M. Tatarakis, A. E. Dangor, X. Fang, P. Graham, T. McCanny, R. P. Singhal, K. W. D. Ledingham, A. Creswell, D. C. W. Sanderson, J. Magill, A. Machacek, J. S. Wark, R. Allott, B. Kennedy, and D. Neely, *Phys. Plasma* **6**, 2150 (1999).
- ¹¹C. Courtois, A. Compant La Fontaine, O. Landoas, G. Lidove, V. Méot, P. Morel, R. Nuter, E. Lefebvre, A. Boscheron, J. Grenier, M. M. Aléonard, M. Gerbaux, F. Gobet, F. Hannachi, G. Malka, J. N. Scheurer, and M. Tarisien, *Phys. Plasmas* **16**, 013105 (2009).
- ¹²T. J. Goldsack, T. F. Bryant, P. F. Beech, S. G. Clough, G. M. Cooper, R. Davitt, R. D. Edwards, N. Kenna, J. McLean, A. G. Pearce, M. J. Phillips, K. P. Pullinger, D. J. Short, M. A. Sinclair, K. J. Thomas, J. R. Threadgold, M. C. Williamson, and K. Krushelnick, *IEEE Trans. Plasma Sci.* **30**, 239 (2002).
- ¹³M. D. Perry, J. A. Sefcik, T. Cowan, S. Hatchett, A. Hunt, M. Moran, D. Pennington, R. Snavely, and S. C. Wilks, *Rev. Sci. Instrum.* **70**, 265 (1999).
- ¹⁴Y. Glinec, J. Faure, L. Le Dain, S. Darbon, T. Hosokai, J. J. Santos, E. Lefebvre, J. P. Rousseau, F. Burgy, B. Mercier, and V. Malka, *Phys. Rev. Lett.* **94**, 025003 (2005).
- ¹⁵C. Courtois, R. Edwards, A. Compant La Fontaine, C. Aedy, M. Barbotin, S. Bazzoli, L. Biddle, D. Brebion, J. L. Bourgade, D. Drew, M. Fox, M. Gardner, J. Gazave, J. M. Lagrange, O. Landoas, L. Le Dain, E. Lefebvre, D. Mastro Simone, N. Pichoff, G. Pien, M. Ramsay, A. Simons, N. Sircombe, C. Stoeckl, and K. Thorp, *Phys. Plasmas* **18**, 023101 (2011).
- ¹⁶T. E. Cowan, A. W. Hunt, T. W. Phillips, S. C. Wilks, M. D. Perry, C. Brown, W. Fountain, S. Hatchett, J. Johnson, M. H. Key, T. Parnell, D. M. Pennington, R. A. Snavely, and Y. Takahashi, *Phys. Rev. Lett.* **84**, 903 (2000).
- ¹⁷K. W. D. Ledingham, I. Spencer, T. McCanny, R. P. Singhal, M. I. K. Santala, E. Clark, I. Watts, F. N. Beg, M. Zepf, K. Krushelnick, M. Tatarakis, A. E. Dangor, P. A. Norreys, R. Allott, D. Neely, R. J. Clarke, A. C. Machacek, J. S. Wark, A. J. Cresswell, D. C. W. Sanderson, and J. Magill, *Phys. Rev. Lett.* **84**, 899 (2000).
- ¹⁸R. J. Clarke, D. Neely, R. D. Edwards, P. N. M. Wright, K. W. D. Ledingham, R. Heathcote, P. McKenna, C. N. Danson, P. A. Brummitt, J. L. Collier, P. E. Hatton, S. J. Hawkes, C. Hernandez-Gomez, P. Holligan, M. H. R. Hutchinson, A. K. Kidd, W. J. Lester, D. R. Neville, P. A. Norreys, D. A. Pepler, T. B. Winstone, R. W. W. Wyatt, and B. E. Wyborn, *J. Radiol. Prot.* **26**, 277 (2006).
- ¹⁹A. Compant La Fontaine, C. Courtois, and E. Lefebvre, *Phys. Plasmas* **19**, 023104 (2012).
- ²⁰L. J. Waxer, D. N. Maywar, J. H. Kelly, T. J. Kessler, B. E. Kruschwitz, S. J. Loucks, R. L. McCrory, D. D. Meyerhofer, S. F. B. Morse, C. Stoeckl, and J. D. Zuegel, *Opt. Photon. News* **16**, 30 (2005).
- ²¹H. M. Abhold and J. S. Hendricks, *Los Alamos National Laboratory Report No. LA 13709-M*, edited by J. F. Briesmeister (2000).
- ²²A. J. Mackinnon, Y. Sentoku, P. K. Patel, D. W. Price, S. Hatchett, M. H. Key, C. Andersen, R. Snavely, and R. R. Freeman, *Phys. Rev. Lett.* **88**, 0215006 (2002).
- ²³Y. Sentoku, T. E. Cowan, A. Kemp, and H. Ruhl, *Phys. Plasmas* **10**, 2009 (2003).
- ²⁴J. Myatt, W. Theobald, J. A. Delettrez, C. Stoeckl, M. Storm, T. C. Sangster, A. V. Maximov, and R. W. Short, *Phys. Plasmas* **14**, 056301 (2007).
- ²⁵P. Neumayer, B. Aurand, M. Basko, B. Ecker, P. Gibbon, D. C. Hochhaus, A. Karmakar, E. Kazakov, T. Kühl, C. Labaune, O. Rosmej, An. Tauschwitz, B. Zeilbauer, and D. Zimmer, *Phys. Plasmas* **17**, 103103 (2010).
- ²⁶C. Courtois, R. Edwards, A. Compant La Fontaine, C. Aedy, S. Bazzoli, J. L. Bourgade, J. Gazave, J. M. Lagrange, O. Landoas, L. Le Dain, D. Mastro Simone, N. Pichoff, G. Pien, and C. Stoeckl, *Phys. Plasmas* **20**, 083114 (2013).
- ²⁷A. Compant La Fontaine, *J. Phys. D: Appl. Phys.* **40**, 1712 (2007).
- ²⁸S. Jacquemot and A. Decoster, *Laser Part. Beams* **9**, 517 (1991).
- ²⁹E. Lefebvre and G. Bonnaud, *Phys. Rev. E* **55**, 1011 (1997).
- ³⁰S. P. Hatchett, C. G. Brown, T. E. Cowan, E. A. Henry, J. S. Johnson, M. H. Key, J. A. Koch, A. B. Langdon, B. F. Lasinski, R. W. Lee, A. J. Mackinnon, D. M. Pennington, M. D. Perry, T. W. Philips, M. Roth, T. C. Sangster, M. S. Singh, R. A. Snavely, M. A. Stoyer, S. C. Wilks, and K. Yasuike, *Phys. Plasmas* **7**, 2076 (2000).
- ³¹F. Perez, L. Gremillet, M. Koenig, S. D. Baton, P. Audebert, M. Chahid, C. Rousseaux, M. Drouin, E. Lefebvre, T. Vinci, J. Rassuchine, T. Cowan, S. A. Gaillard, K. A. Flippo, and R. Shepherd, *Phys. Rev. Lett.* **104**, 085001 (2010).
- ³²F. N. Beg, A. R. Bell, A. E. Dangor, A. P. Fews, M. E. Glinisky, B. A. Hammel, P. Lee, P. A. Norreys, and M. Tatarakis, *Phys. Plasmas* **4**, 447 (1997).
- ³³M. G. Haines, M. S. Wei, F. N. Geg, and R. B. Stephens, *Phys. Rev. Lett.* **102**, 045008 (2009).
- ³⁴A. Compant La Fontaine, "Photon dose produced by a high intensity laser on a solid target," *J. Phys. D: Appl. Phys.* (to be published).
- ³⁵N. J. Carron and C. L. Longmire, *IEEE Trans. Nucl. Sci.* **23**, 1986 (1976).
- ³⁶P. L. Shkolnikov, A. E. Kaplan, A. Pukhov, and J. Meyer-ter-Vehn, *Appl. Phys. Lett.* **71**, 3471 (1997).
- ³⁷J. Galy, M. Maučec, D. J. Hamilton, R. Edwards, and J. Magill, *New J. Phys.* **9**, 23 (2007).
- ³⁸A. L. Meadowcroft and R. Edwards, *IEEE Trans. Plasma Sci.* **40**, 1992 (2012).
- ³⁹C. D. Chen, J. A. King, M. H. Key, K. U. Akli, F. N. Beg, H. Chen, R. R. Freeman, A. Link, A. J. Mackinnon, A. G. MacPhee, P. K. Patel, M. Porkolab, R. B. Stephens, and L. D. Woerkom, *Rev. Sci. Instrum.* **79**, 10E305 (2008).
- ⁴⁰D. J. S. Findlay, *Nucl. Instrum. Methods Phys. Res. A* **276**, 598 (1989).
- ⁴¹M. Abramowitz and I. Stegun, *Handbook of Mathematical Functions* (Dover Publication, INC., N.Y., 1970).
- ⁴²K. Kamaya and S. Okayama, *J. Phys. D: Appl. Phys.* **5**, 43 (1972).
- ⁴³L. Katz and A. S. Penfold, *Rev. Mod. Phys.* **24**, 28 (1952).
- ⁴⁴W. Heitler, *The Quantum Theory of Radiation* (Oxford, Clarendon Press, 1954).
- ⁴⁵Y. Garcier, G. Cordier, C. Pauron, and J. Fazileabasse, *Radiat. Prot. Dosim.* **124**, 107 (2007).
- ⁴⁶J. Howe, D. M. Chambers, C. Courtois, E. Förster, C. D. Gregory, I. M. Hall, O. Renner, I. Uschmann, and N. C. Woolsey, *Rev. Sci. Instrum.* **77**, 036105 (2006).